Corrosion Science 100 (2015) 73–84

Contents lists available at ScienceDirect

Corrosion Science

journal homepage: www.elsevier.com/locate/corsci

The coupled current charge compensation model for zirconium alloy fuel cladding oxidation: I. Parabolic oxidation of zirconium alloys

Adrien Couet [a,b,*], Arthur T. Motta [a], Antoine Ambard [b]

[a] Department of Mechanical and Nuclear Engineering, Penn State University, University Park 16802, PA, USA
[b] EDF Research and Development, Materials and Mechanics of Components, Ecuelles, 77818 Moret-sur-Loing, France

ARTICLE INFO

Article history:
Received 17 October 2014
Received in revised form 15 July 2015
Accepted 19 July 2015
Available online 26 July 2015

Keywords:
Zirconium
XANES
Oxidation
High temperature corrosion

ABSTRACT

A first principles oxidation model has been developed which can rationalize the kinetics observed in various zirconium alloys using a unified theoretical approach, which predicts that space charges in the oxide have a major impact on oxidation kinetics. As a first development, the parabolic oxidation of Zr–0.4Nb alloy is fitted by the model assuming that space charges in the oxide are compensated by Nb ions. The model quantitatively reproduces the oxidation kinetics using physically significant parameters. XANES examinations show that there are enough aliovalent Nb ions in the oxide layer to verify oxide electroneutrality as predicted by the model.

1. Introduction

Uniform corrosion of zirconium alloy fuel cladding and the associated hydrogen pickup is a potential life-limiting degradation mechanism for nuclear fuel cladding in existing and advanced light water reactors especially for the higher fuel duties currently used in the industry. It is thus of interest for fuel vendors to limit waterside corrosion by developing alloys that are more resistant to corrosion than the ones in current use. Optimization of alloying element composition is one of the key factors to increasing corrosion resistance in zirconium based alloys. In the initial pre-transition regime of water-side corrosion at 360 °C the oxidation of zirconium alloy fuel cladding can be described by a power law:

$$\delta(t) = kt^n \quad (1)$$

with δ the oxide thickness and t the exposure time [1]. This protective regime persists until the oxide transition, defined as the stage in the corrosion process at which a sudden increase in corrosion rate occurs ($\delta \sim 2$–$3\ \mu m$). The post-transition regime can be divided into several periods of corrosion that cyclically reproduce the pre-transition regime. Fig. 1 shows such oxidation behavior for a Zr–1.0Nb alloy corroded in a 360 °C pure water autoclave (see [2] for experimental details). The pre-transition and 1st transition regimes have been fitted to a power law such as Eq. (1).

Careful analysis of the pre-transition oxidation kinetics of zirconium alloys has shown a range of value of n from as low as $n \sim 0.2$ for ZrCu, to $n \sim 0.3$ for Zircaloy-type alloys and as high as $n \sim 0.5$ for ZrNb alloys [2–4]. This range of sub-parabolic kinetics deduced from power law fitting of oxidation kinetics in the pre-transition regime is obtained on alloys that have very small differences in their alloying content. This is rather uncommon in metal oxidation theory and the underlying mechanism is still not well understood [5]. It is important to note that the value of n is related to the alloy composition, such that Zr–Nb alloys generally exhibit close to parabolic oxidation kinetics [4,6] (see Fig. 1), whereas Zircaloys exhibit behavior closer to cubic or even sub-cubic kinetics ($n \leq 0.3$) [7–10]. Although the parameter n in these fits is not easily derivable from existing theories of metal oxidation, its reproducibility for the alloys studied is a clear phenomenological evidence of a consistent mechanistic deviation from the oxidation mechanism derived by Hauffe and Wagner, which predicts parabolic growth of thick oxides [5,11].

The purpose of this study is to investigate physical reasons for these differentiated oxidation kinetics in various zirconium alloys and to create a model that describes this kinetics. The model is then applied to the particular oxidation behavior of Zr–0.4Nb, which shows nearly parabolic behavior in the pre-transition regime.

* Corresponding author.
E-mail address: adrien.couet@gmail.com (A. Couet).

http://dx.doi.org/10.1016/j.corsci.2015.07.003
0010-938X/

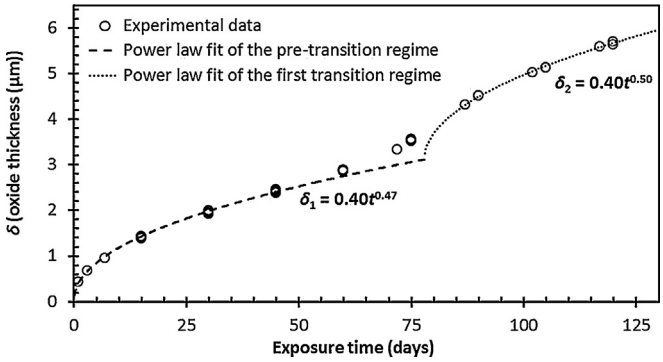

Fig. 1. Oxide thickness (in μm) of Zr–1.0Nb annealed at 720 °C as function of exposure time in a 360 °C autoclave in pure water at 180 MPa. The power law fits of the pre-transition and 1st transition regime are also plotted along with the corresponding equations [4].

2. Review of zirconium alloys corrosion mechanism

2.1. Review of metal oxidation theories

The oxidation of metals has been extensively modeled since the pioneering work of Wagner [11]. The oxide layer is generally considered homogeneous, that is, without shortcuts such as pores or grain boundaries for diffusive species to migrate through the layer. Although models of preferential diffusion through grain boundaries exist [12,13] consistent results can be obtained without recourse to this hypothesis.

The model for the formation of a protective oxide consists of a system of partial differential equations describing:

1. The mobility of the interfaces (metal-oxide and oxide-solution) in relation with the fluxes of atomic species and the growth of the oxide layer.
2. The mobility of the chemical species in the oxide layer under the action of various driving forces.
3. The boundary conditions at the interface (fixed concentrations, fixed flux, mixed conditions).
4. The list of the diffusive species (atoms, cations, anions, electrons, holes, vacancies, charged vacancies...).

Although oxidation can be limited by the interface reaction (by the flux of the species at the interface), in the following we assume that the rate limiting step is diffusion–migration[1] through the oxide. One justification for this assumption is that the corrosion rate decreases with increasing oxide thickness, which would not be observed if a surface reaction was rate limiting.

Models are often based on the *steady state approximation*: calculations are performed with fixed interface and time derivatives set to 0 [11]. The unknowns are the concentrations of the species in the oxide layer, their fluxes and the electric field. In such models the growth of the oxide layer is calculated using the flux of species at the interfaces.

Models also differ by the *mobility equation* in the oxide layer either *linear* (Nernst–Planck equation with the Einstein relation linking diffusivity to electrical mobility) or *non-linear*. Models that neglect diffusion–migration or electric field induced mobilities can be seen as special cases of the more general model, which takes into account both driving forces [14]. Non-linearity can arise because of either chemical diffusion (when the activity coefficient differs from unity) or from the dependence on the electric field (exponential dependence when the electric field across the oxide layer is relatively high).

Experiments show that no net current crosses the oxide layer. This has been modeled by setting the sum of the currents to 0 at all locations in the oxide (the so-called *coupled current* hypothesis) [15] or by imposing the *electroneutrality* of the oxide [16–18]. The latter is more restrictive than the former and is equivalent to assuming a constant electric field in the oxide. Finally, *boundary conditions* must also be imposed, specifying the concentrations and fluxes of the various chemical species as well as the potential. Additionally, non-steady state modeling of oxidation requires *initial conditions*.

Table 1 provides a review of various oxidation models according to these criteria. It must be noted that few of these models have been applied to zirconium oxidation (see references in Table 1). The model developed in this study is derived from Fromhold [19,20] and applied to zirconium oxidation. A brief summary of zirconium oxidation models developed in the literature is presented in the following.

2.2. Review of zirconium oxidation models

Assuming that oxygen diffusion–migration is rate-limiting, hypotheses explaining the observed sub-parabolic kinetics of zirconium alloys simply based on oxygen atoms diffusion under a concentration gradient (Fick's law) have been proposed in the literature such as grain boundary diffusion combined with a linear change in the grain size [21], the effect of a gradient of compressive stresses in the oxide [22,23], or the development of barriers for oxygen diffusion during oxide growth such as pores or cracks [10].

The above hypotheses are based on a corrosion mechanism controlled by oxygen anion transport and an alteration of this transport as the oxide grows is then proposed to explain sub-parabolic kinetics. This model implicitly assumes that all other reactions including electron transport in the oxide layer and interfacial reactions are fast compared to oxygen diffusion. However these assumptions are not yet proven [24–29]. Furthermore none of these hypotheses address the predominant charge state of the oxygen vacancy (or oxygen anion), the incorporated aliovalent alloying elements in the oxide or the existence of an electric field across the oxide.

To properly model the oxidation mechanism of zirconium alloys it is necessary to take into account (i) the electric field generated by charged point defect gradients and (ii) the necessary coupled cathodic current (e.g. electron current), which is equal in magnitude but opposite in sign to the anionic current so that the net current across the oxide is zero. It is indeed necessary to verify the overall zero current condition in the oxide such that the oxygen anion flux is balanced by the electron flux in the opposite direction (and potentially by an additional proton flux responsible for hydrogen pickup [2,30]). Despite extensive experimental effort [31], the existence of an oxygen concentration gradient across the oxide acting as a primary driving force for oxygen diffusion and oxide growth has not been directly measured, even though the observed black or gray color of the protective oxide suggests that the ZrO_2 layer formed is sub-stoichiometric. It is also well known that thick zirconium oxide films can be formed simply by anodic polarization [32,33] so that charged species are part of the corrosion process. It is thus necessary to consider both the effect of electron transport and the presence of the electric field to grow micrometer-sized oxides during thermal oxidation [1,33,34]. In that sense, space charge theory can explain sub-parabolic kinetics [19]. Only a few studies have attempted to apply this theory to zirconium oxidation [35,36], even though their results are convincing. Indeed, the authors reproduced Zircaloy-4 pre-transition cubic oxidation kinetics assuming that space charges are created by doping of ZrO_2 by Fe and Cr

[1] The term diffusion–migration refers to the motion of charged atomic species in the oxide layer, driven by both concentration gradients (Fick's law) and by electric field gradients.

Table 1
Classification of various oxidation models according to their hypothesis. "No" in a cell means that the model is using the other hypothesis. For example "no electroneutrality" means that the model used the coupled current hypothesis.

Models	Steady-state	Linear mobility equation	Local electroneutrality	Boundary conditions = fixed concentrations/potential	Diffusive species	Remarks
Wagner [11]	Yes	Yes	Yes	Yes	No restrictions	Local equilibrium between defects and atoms
Mott [74]	Yes	No	Yes	No	Cations Electrons	Chemical diffusion is neglected in the mobility equation Electroneutrality is not formally in the model but electric field is constant Rate limiting step is atom flux at the interface.
Mott-Cabrera/high field model – thin oxide [75]	Yes	No	No	No		
Fromhold[a] [19]	Yes	No	No	Yes	No restriction	Only in some specific cases one can get an analytical solution
Evans [22]	Yes	No	Yes	Yes	Double-charged oxygen vacancies The specie providing electroneutrality is not specified.	Electric field is not taken into account in the mobility equation. Non-linearity arises from the stress and the activity coefficient.
Point Defect Model[b] [16,17]	Yes	Yes	Yes	Yes	Charged cations and anions vacancies Electrons Interstitials	Dissolution of the oxide in the solution is taken into account Electroneutrality is not formally part of the model but electric field is constant throughout the oxide. Interfacial reactions are taken into account
Mixed Conduction Model [18]	Yes	No	Yes	No	Charged cations and anions vacancies Electrons	Potential drops across the interfaces are modeled and electron current is explicitly taken into account
Generalized Model [76,77]	Yes	No	Yes	No	Charged cations and anions vacancies	
Diffusion Poisson Coupled Model [78,79]	No	Yes	No	No	Potentially no restrictions	Non steady state assumption is useful to describe abrupt transients conditions but probably not necessary for uniform corrosion as studied here

[a] In his book, Fromhold describes numerous models of oxidation, starting from the simplest one and ending with the most complicated one. The table refers to the latter (chapter 8 in [20]).
[b] According to the nomenclature proposed by Macdonald [17].

alloying elements, which would create oxygen anion vacancies in the oxide layer.

To address this problem, the application of space charge theory to zirconium oxidation by the development of the Coupled Current Charge Compensation (C4) model based on Fromhold's framework is investigated in this study. A special case of the model is solved in which space charge compensation by embedded Nb aliovalent ions is assumed and the consequences of this assumption are clearly detailed. This assumption is validated for actual experiments by data from microbeam XANES experiments, as detailed in the last part of the paper. A mechanism of zirconium alloy oxidation resulting from the model is discussed.

3. Coupled Current Charge Compensation (C4) model

The overall objectives of the C4 model are (i) to provide a rationale for the observed sub-parabolic oxidation kinetics and (ii) to rationalize corrosion differences between alloys. The model arrives at the oxidation kinetics by solving the *mobility* equations for the atomic species traveling in the oxide layer under the concentration and electric potential driving forces using the hypotheses discussed in the following.

3.1. Model assumptions

The model is derived from the following hypotheses:

1. Only the transport of doubly-charged oxygen vacancies ($V_{\ddot{O}}$ using Kroger–Vink notations) and electrons (e^-) is considered. Zirconium oxide is known to be a n-type semiconductor [3,37,38] and it is well established that the cation transport number is close to zero at normal operating conditions (360 °C, 180 MPa), which means that Zr atoms do not diffuse outward in the oxide layer [39] and the oxygen anion is the only diffusing ion in the oxide (inward proton diffusion related to the hydrogen flux is not yet considered) [40,41]. The vacancy diffusion–migration mechanism hypothesis is also well established for corrosion of zirconium alloys at normal operating conditions [18].
2. The one-dimensional conservation law applied for both oxygen vacancies and electrons can be written as follows:

$$\frac{\partial J_s(x,t)}{\partial x} + \frac{\partial C_s(x,t)}{\partial t} = 0 \tag{2}$$

with $s = e^-, V_{\ddot{O}}$, J_s the flux of the species s in $m^{-2}\,s^{-1}$ and C_s the concentration of the species per unit volume in m^{-3}. We assume steady state, so that, from Eq. (2), J_s is also independent of x (this has been found to be correct in the pre-transition regime [10]). The steady-state hypothesis implies that all transients disappear before the formation of a new oxide monolayer. In this limit the currents of the individual atomic species are uniform throughout the oxide layer, with sources and sinks only at the interfaces and the interfacial potentials are at equilibrium before the formation of a new oxide monolayer. This hypothesis is verified as detailed in Appendix A.
3. The concentrations of species at the interfaces are fixed during the exposure time. This implies that the vacancy formation and the hydrogen evolution interface reactions are at equilibrium, the surface reactions being much faster than the transport of species across the oxide. The concentration values are imposed by the structure of the oxide/metal interface and by the Nernst equilibrium. The diffusion–migration of species across the oxide as the rate-limiting step has indeed been confirmed experimentally [10,42]. Also, the fact that oxidation kinetics depend on oxide thickness is an additional evidence of the diffusion–migration of species being rate-limiting.
4. A direct consequence of the last hypothesis is that the interfacial potential drops are independent of oxide thickness, so that only the potential drop across the oxide varies as a function of oxide thickness Thus, the interfacial reactions are under steady-state conditions. This is supported by the following:
   a. Microstructural and (electro)-chemical characterizations of the oxide/metal interface show no significant variations with exposure time [4,43]. Since the electron injection into the ZrO_2 conduction band depends on the energy difference between the Fermi levels in both phases [25], it is assumed that the electron flux at the oxide/metal interface is constant.
   b. The zirconium open circuit potential measured in situ during corrosion of zirconium alloys shows no significant variations as function of exposure time [36,44–47] remaining stable at least until oxide transition. It is thus likely that the electric field decreases as the oxide thickens whereas the potential drop across the oxide remains constant.
   c. The overpressure of hydrogen during zirconium oxidation shows no significant effect on oxidation kinetics up to at least 2000 psi [48,49]. Thus the electrochemical potential fixed by hydrogen partial pressure in the electrolyte does not significantly affect the oxidation kinetics.

   These results indicate that, to a first approximation the thermodynamic conditions at the interfaces are constant.
5. The diffusion of oxygen into the metal ahead of the oxide (for example to form sub-oxides ahead of the main oxide front [50]) does not significantly affect oxide growth. Although this may be a strong assumption, it is taken as the simplest initial assumption of the model.
6. The oxide-water and oxide-metal interfaces are planar. The waviness of the oxide/metal interface often observed in SEM is not considered.
7. The coupled-current condition of net zero charge transport through the film at all times is imposed:

$$\sum_{s}^{\text{diffusing species}} Z_s e J_s = 0 \tag{3}$$

with Z_s the valence of the species s and e the electron charge in C.

3.2. Formulation of the Coupled Current Charge Compensation model

Using the above hypotheses the formulation of the general corrosion model to be solved is as follows:

1. The one-dimensional *mobility* equation relating the fluxes to the electric field and charged species concentrations is taken from Fromhold [20]. This relation is defined as:

$$J_s = g(E, C_s) \tag{4}$$

where g is an integral function defined in Appendix B. The diffusion–migration equation is recovered from decomposing the oxide layer into a lattice consisting of N potential barriers of height E_m^s for the sth diffusing species located at $x_k = (2k-1)a$, $k = 1, \ldots, N$, with $2a$ representing the jump distance between two potential minima. The scheme is depicted in Fig. 3 and the formulation is developed in Appendix B.
2. Poisson's equation expresses the electric charge density ρ as a source of electric field relating the charged species concentration to the local electric field:

$$\frac{\partial E(x,t)}{\partial x} - \frac{\rho}{\varepsilon\varepsilon_0} = 0 \tag{5}$$

with E the electric field in $V\,m^{-1}$, ε the relative permittivity of ZrO_2 and ε_0 the vacuum permittivity in $F\,m^{-1}$.

3. The coupled current equation (3) is verified:

$$2J_{V_{\ddot{O}}} - J_{e^-} = 0 \tag{6}$$

4. The relationship between the vacancy flux and the oxide thickness is given by:

$$\frac{\Delta\delta}{\Delta t} = f(J_{V_{\ddot{O}}}) \tag{7}$$

where f is a function defined in Appendix B.

5. The boundary conditions are the concentrations of charged species at the interfaces ($x=0$ is the oxide/metal interface and $x=\delta$ is the oxide/water interface position).

For a given oxide thickness, the system of equation to solve is as follows:

$$\begin{cases} \text{Unknown :} & \text{oxygen flux at the metal oxide interface} \\ \text{Intensity–Potential law :} & J_s = g(E(x), C_s(x)) \\ \text{Maxwel–Gauss equation :} & \dfrac{\partial E(x)}{\partial x} - \dfrac{\rho(x)}{\varepsilon\varepsilon_0} = 0 \\ \text{Coupled current equation :} & 2J_{V_{\ddot{O}}} - J_{e^-} = 0 \\ \text{Boundary condition :} & C_{V_{\ddot{O}}}(\delta), C_{e^-}(\delta), C_{V_{\ddot{O}}}(0), C_{e^-}(0) \end{cases}$$

The thickness increment for a time increment Δt is calculated using:

$$\Delta\delta = f(J_{V_{\ddot{O}}})\Delta t \tag{8}$$

3.3. Particular case of parabolic oxidation: ZrNb alloys

As stated before, ZrNb alloys tend to exhibit close to parabolic behavior. Parabolic oxidation supposes that electroneutrality is verified locally [15], so that:

$$\rho(x) = 0 \Leftrightarrow \sum_{s}^{\text{All species}} Z_s C_s(x) = 2C_{V_{\ddot{O}}}(x) - C_{e^-}(x) + \sum_{i}^{\text{Aliovalent ions}} Z_i C_i(x) = 0 \tag{9}$$

Eq. (9) is used in the rest of this study since it concerns parabolic oxidation. Under the electroneutrality hypothesis, Eq. (3) actually reduces to the less general case of Eq. (9). The two equations have been derived to emphasize that the model can take into account the effect of local space charges. However, in the particular case of ZrNb parabolic oxidation studied here, it is assumed that Nb ions embedded in the oxide compensate any charge differences arising from diffusing species so that Eq. (10) is verified

$$2C_{V_{\ddot{O}}}(x) - C_{e^-}(x) + Z_{Nb^{m+}} C_{Nb^{m+}}(x) = 0 \tag{10}$$

The model does *not* assume $2C_{V_{\ddot{O}}} = C_{e^-}$. Indeed, it is assumed that aliovalent ions, which are *not* part of the diffusion–migration process, are present in the oxide and compensate space charges resulting from the diffusion of electrons and vacancies. This major hypothesis has been actually validated by XANES measurements as detailed in Section 5.2. Using the system of equations detailed previously, the fluxes are derived as function of the boundary conditions and the homogeneous electric field E_0 in Appendix B. In Eq. (B.6), E_0 results from the ambipolar diffusion–migration of charged species and is sometimes called *homogeneous field* [15].

Starting from Eq. (B.6) in Appendix B and assuming equation (10) is verified, one can evaluate the sum in Eq. (B.7). Combining Eqs. (B.6) and (B.7), the following equation (sometimes referred to as the Fromhold–Cook equation [51]) for the flux is obtained:

$$J_s = 4a\nu_s e^{-((eE_m^s)/k_BT)} \sinh\left(\frac{Z_s eE_0 a}{k_B T}\right) \frac{\left(C_0^s - C_N^s e^{((2Z_s eaNE_0)/(k_B T))}\right)}{\left(1 - e^{-((2Z_s eaNE_0)/(k_B T))}\right)} \tag{11}$$

Assuming that:

$$\sinh\left(\frac{Z_s eE_0 a}{k_B T}\right) \sim \frac{Z_s eE_0 a}{k_B T} \Leftrightarrow E_0 \ll \frac{k_B T}{ea} \Leftrightarrow E_0 \ll 10^6\,V/cm \tag{12}$$

which is generally valid for thick oxide growth [52], Eq. (11) can be rewritten and the well-known linear diffusion–migration equation is retrieved:

$$J_s = \mu_s E_0 \frac{(C_N^s - C_0^s e^{-((\mu_s \delta E_0)/D_s)})}{(1 - e^{-((\mu_s \delta E_0)/D_s)})} \tag{13}$$

where

$$\mu_s = \frac{eZ_s D_s}{k_B T} \tag{14}$$

$$D_s = 4a\nu_s e^{-(E_m^s/(k_B T))} \tag{15}$$

μ_s is the mobility coefficient in $cm^2\,V^{-1}\,s^{-1}$ and D_s is the diffusion coefficient in $cm^2\,s^{-1}$.

This derivation represents a particular case of the C4 model for which Eq. (10) is verified by the presence of Nb aliovalent ions. The particularity of this development is that, even though $|Z_{V_{\ddot{O}}}| \neq |Z_{e^-}|$ and $|Z_{V_{\ddot{O}}}| > 1$, an analytical solution can be obtained for the case of doubly charged vacancy and electron transport (see Appendix C), such that the oxidation kinetics follows an exact parabolic law $\delta(t) = kt^{0.5}$ and that this parabolic behavior is observed independently of the chosen parameters.

4. Choice of parameters and code optimization

The model requires eight different input parameters: the concentrations of vacancies and electrons at the two interfaces ($C_0^{e^-}$; $C_N^{e^-}$; $C_0^{V_{\ddot{O}}}$; $C_N^{V_{\ddot{O}}}$), the migration energies for electrons and vacancies in the oxide $E_m^{e^-}$ and $E_m^{V_{\ddot{O}}}$, the migration jump distance a and the temperature T. The temperature is set at $T = 633$ K and the jump distance for particle migration is set at $a = 0.5$ nm. This distance is of the order of the lattice parameter of monoclinic ZrO_2 [53]. The distance between localized electron traps is assumed of the same order of magnitude [54]. Thus, for the sake of simplicity, the same jump distance is used both for electron untrapping and vacancy migration. A systematic sensitivity study of the $C_0^{e^-}$, $C_N^{e^-}$; $C_0^{V_{\ddot{O}}}$, $C_N^{V_{\ddot{O}}}$, $E_m^{e^-}$ and $E_m^{V_{\ddot{O}}}$ parameters above was performed and which indicates that of these six parameters $E_m^{e^-}$ and $E_m^{V_{\ddot{O}}}$ are those that most strongly affect the results, whereas the other parameters have comparatively less influence. Therefore, the migration energies were taken as the fit parameters in this study, as detailed in the fitting procedure. The Zr–0.4Nb alloy oxidation kinetics (shown in Fig. 2) is taken as the experimental data to be fitted.

It is assumed that the concentration of electrons and vacancies at the oxide/water interface is negligible so that $C_N^{V_{\ddot{O}}} \sim C_N^{e^-} = 10^{17}$ particles cm^{-3} (the number density of oxygen atoms in stoechiometric ZrO_2 is equal to 5.55×10^{22} atoms cm^{-3}). The ZrO_2 molecular volume is given by:

$$R_v \sim \frac{M_{ZrO_2}}{\rho_{ZrO_2} \times N_A} = 2.67 \times 10^{22}\,cm^3/\text{molecules} \tag{16}$$

where the zirconia molar mass $M_{ZrO_2} = 123.2\,g\,mol^{-1}$, the zirconia density ρ_{ZrO_2} is $5.68\,g\,cm^{-3}$ and N_A is Avogadro's number.

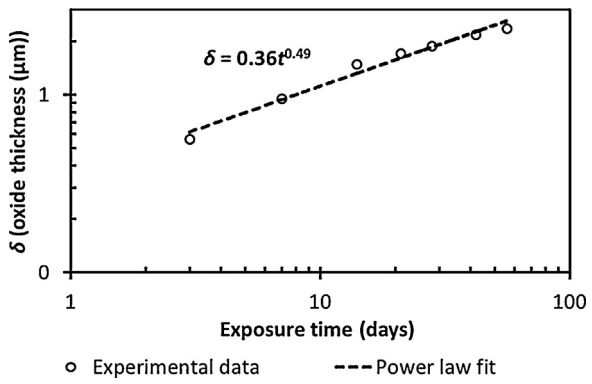

Fig. 2. Oxide thickness (in μm) of Zr–0.4Nb alloy as function of exposure time (in days) in a 360 °C autoclave in pure water at 180 MPa. The power law fit is also plotted along with the corresponding equation [4].

Thermodynamic data predicts a sub-stoichiometry of 0.75% ($ZrO_{1.985}$) [55], corresponding to 66.17 at%, as compared to the stoichiometric 66.66 at%. This amount of sub-stoichiometry is rather small, which may explain why this oxygen deficiency has yet to be measured experimentally [31]. Because the model is not very sensitive to the concentrations at the oxide/metal interface the exact value of the sub-stoichiometry is not critical to the results. If we assume a sub-stoichiometry of 0.75% at the oxide/metal interface ($ZrO_{1.985}$), then $C_0^{V_{\ddot{O}}} \sim 4.2 \times 10^{20}$ vacancies cm^{-3}. The electron concentration at the oxide/metal interface is chosen to compensate the charge so that $C_0^{e^-} \sim 8.4 \times 10^{20}$ electrons cm^{-3}.

As mentioned above, the electron untrapping energy $E_m^{e^-}$ and vacancy migration energy $E_m^{V_{\ddot{O}}}$ will be used as fitting parameters. In many electrochemical measurements available in the literature, electron transport mechanism theories have been fitted to I-V curves to estimate $E_m^{e^-}$ (see refs in Table 2), but no general agreement on the value of $E_m^{e^-}$ has been reached. In order to determine the range of possible values for these two parameters, the oxide thickness after 75 days of exposure was chosen for optimization:

$$1.5\,\mu m < \delta_{opt} < 3.5\,\mu m \quad (17)$$

Table 2
Electron untrapping energy $E_m^{e^-}$ (in eV) for various zirconium alloy corrosion found in the literature.

$E_m^{e^-}$ (eV)	Reference
$0.2 < E_m^{e^-} < 0.4$	[54,80]
$0.2 < E_m^{e^-} < 2$	[27]
0.5	[81]
0.65	[61]
$0.2 < E_m^{e^-} < 1$	[59]
$0.3 < E_m^{e^-} < 1.1$	[58]

This range covers most of the oxidation kinetics of zirconium alloys observed in a protective regime [4]. The purpose is to find for which values of the ($E_m^{e^-}$, $E_m^{V_{\ddot{O}}}$) couples equation (17) is verified. The results are plotted in Fig. 4 as a contour plot in which E_m^s are along the x and y axis whereas δ_{opt} is along the z axis. The contour lines for 0.5 μm, 1.5 μm, 3.5 μm, 10 μm and 100 μm have been plotted. One can draw the conclusion that in order to grow oxide layers of thickness in the range of δ_{opt}, the values of the ($E_m^{e^-}$, $E_m^{V_{\ddot{O}}}$) couples have to verify:

$$E_m^{e^-} < 1.58\,eV \text{ and } E_m^{V_{\ddot{O}}} < 1.63\,eV \quad (18)$$

If the E_m^s values exceed these limits, the anodic current resulting from oxygen ion migration would be too small and the resulting oxide thickness could not match the ones observed experimentally. It is interesting to notice that, because the model takes into account both cathodic and anodic currents, the current coupling implies that, if $E_m^{e^-} > 1.58$ eV the oxide growth is equally limited, no matter how small $E_m^{V_{\ddot{O}}}$ is.

It is well known that the energy band gap of monoclinic ZrO_2 is rather large (approximately 4.5 eV [56]). Since, in order to grow micrometer oxide scales, $E_m^{e^-}$ has to be smaller than 1.58 eV, it is believed that electron conduction in the oxide layer arises from thermal ionization of shallow donor states or centers into the conduction band followed by relaxation into empty energy states in the band gap [57,58] rather than from a valence-to-conduction band mechanism. The chemical nature of these centers cannot be easily determined from electrochemical measurements but previous studies have identified this chemical nature as oxygen defects in the band gap [18,27,58–61]. Of particular interest is the oxygen

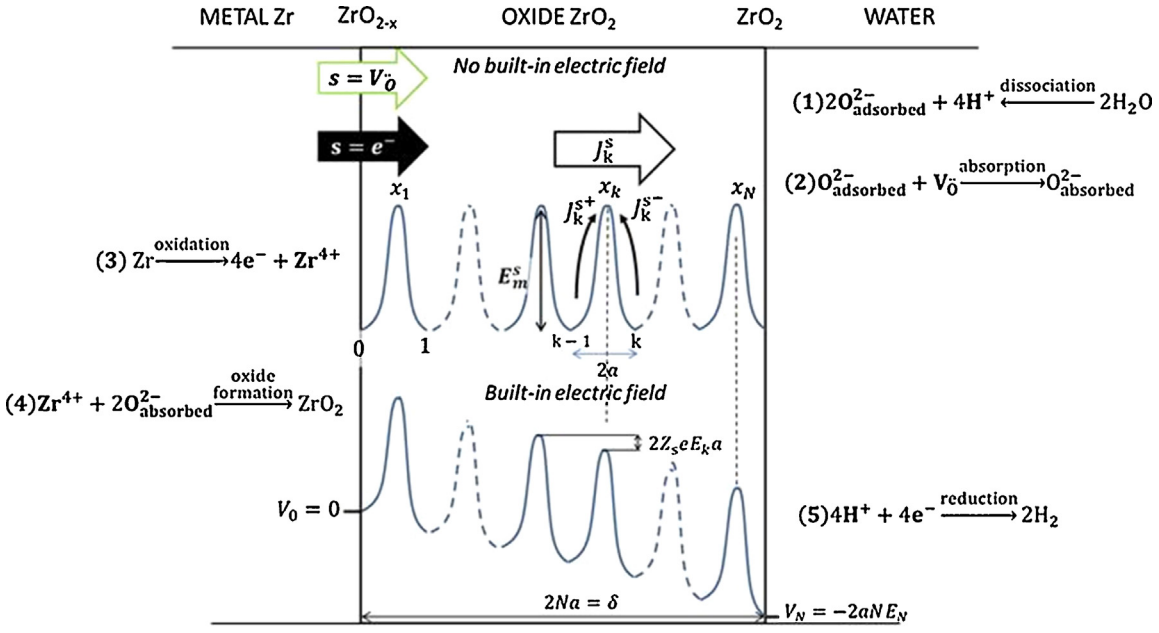

Fig. 3. Scheme of the discrete lattice and the effect of the built-in electric field on the potential energy diagram. The oxidation process can be conceptually divided into several steps from (1) to (5) as presented in [30].

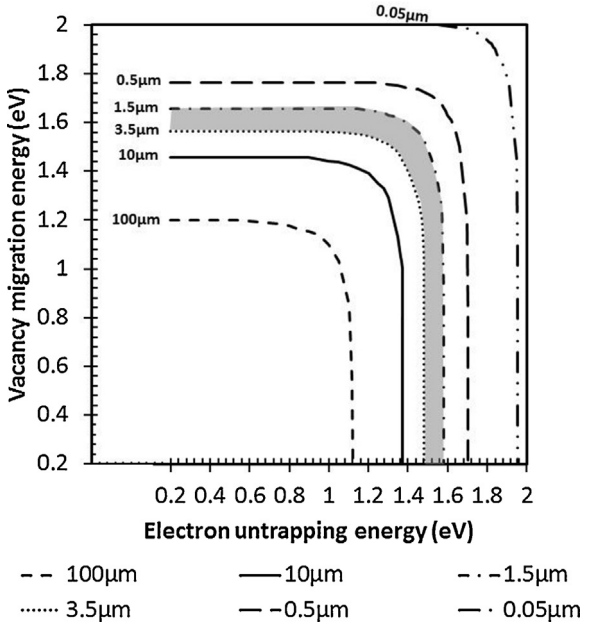

Fig. 4. Contour plot of δ_{opt} as function of $E_m^{V_{\ddot{O}}}$ and $E_m^{e^-}$ (in eV). The contour lines correspond to 0.05 µm, 0.5 µm, 1.5 µm, 3.5 µm, 10 µm and 100 µm oxide thickness. The shaded region corresponds to the inequality (17).

vacancy energy defect level located at approximately 0.8 eV for $V_{\ddot{O}}$ and 1.2 eV for $V_{\dot{O}}$ from the zirconia conduction band [56,61]. It appears reasonable to consider that oxygen anion vacancies act as local traps for electrons at an energy just below the conduction band, thus promoting the transport of electrons [62,63]. Even though there is an energy distribution of such traps rather than a single localized state below the conduction band, as a first attempt $E_m^{e^-}$ is set at an average value of 1 eV. Even if the resulting mobility $\mu_m^{e^-}$ equal to 2×10^{-8} cm^2 V^{-1} s^{-1} is rather low compared to that of other semi-conductors, it is in very good agreement with the literature on zirconium corrosion [27,59].

As an independent check, it is interesting to compare the upper limit to $E_m^{V_{\ddot{O}}}$ from this model, obtained from the diffusion–migration of charged species, to the $E_m^{V_{\ddot{O}}}$ in the case of oxide growth due to diffusion of neutral oxygen atoms solely under a concentration gradient (Fick's law). Using the same parameters, a value of 1.44 eV for $E_m^{V_{\ddot{O}}}$ is calculated to grow an oxide 3.5 µm thick. Thus, if the electric field and the cathodic current are included in the model, the available spectrum of $E_m^{V_{\ddot{O}}}$ is larger (see Eq. (18)). This was expected because $\mu_{V_{\dot{O}}} \ll \mu_{e^-}$ so that the homogeneous field is positive and lowers the energy barrier height for vacancy diffusion–migration by an amount $\alpha = 2aeE_0$. Consequently, a larger $E_m^{V_{\ddot{O}}}$ spectrum is available for a similar anodic current if the electric field is modeled. In conclusion, the sanity check validates the upper value of $E_m^{V_{\ddot{O}}}$.

The $E_m^{V_{\ddot{O}}}$ upper limit is smaller than the activation energy of oxygen vacancy diffusion $E_a^{V_{\ddot{O}}} = 2.3$ eV in ultrafine ZrO_2 grains determined with tracer experiments [64] and is in agreement with the experimental and modeling results presented in [62,65]. Activation energy includes both formation and migration energies. In sub-stoechiometric ZrO_2, the vacancies are already present in sufficient concentrations such that only the oxygen vacancy migration energy is necessary to activate diffusion. In order to estimate $E_m^{V_{\ddot{O}}}$ for parabolic oxidation of ZrNb alloys, the oxidation model has been fitted to the oxidation kinetics of Zr–0.4Nb. The fit gives $E_m^{V_{\ddot{O}}} =$ 1.58 eV, which is in agreement with the literature, as discussed previously. The experimental power law fit (dotted line) and the oxidation model (full line) are plotted in Fig. 5, showing very good agreement. Thus, the Zr–0.4Nb oxidation kinetics has been correctly and quantitatively reproduced using physically significant

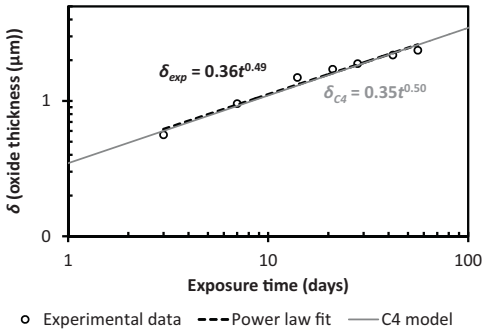

Fig. 5. Oxidation kinetics of Zr–0.4Nb alloy along with the power law fit (dotted black curve) and the oxidation model results (full line) developed in this paper.

Table 3
Values of the different parameters chosen to model Zr–0.4Nb oxidation kinetics.

Parameters	Value
Electron untrapping energy ($E_m^{e^-}$)	1 eV
Vacancy migration energy ($E_m^{V_{\ddot{O}}}$)	1.58 eV
Migration distance (a)	5 Å
Temperature (T)	633 K
Concentration of vacancies at the O/M interface ($C_{V_{\dot{O}}}(0)$)	4.2×10^{20} vacancies/cm^3
Concentration of electrons at the O/M interface ($C_{e^-}(0)$)	8.4×10^{20} electrons/cm^3
Concentration of vacancies at the O/W interface ($C_{V_{\dot{O}}}(\delta)$)	10^{17} vacancies/cm^3
Concentration of electrons at the O/W interface ($C_{e^-}(\delta)$)	10^{17} electrons/cm^3

parameters and assuming that the space charges in the oxide are either negligible or compensated.

The different parameters are summarized in Table 3 and the results of the model are discussed in the next section.

5. Results and discussion

5.1. Results of the Coupled Current Charge Compensation Model

One of the results of the model is the shape of the electric field as function of exposure time plotted in Fig. 6. The effect of the electric field on the anionic current is also shown in Fig. 6 where the vacancy fluxes from the model and from Fick's law derivation are plotted as function of exposure time. As expected, the vacancy flux in the C4 model is higher than that from Fick's law because of the positive homogeneous electric field. The homogeneous electric field is lower than 10^6 V/cm, such that Eq. (12) is verified, validating the use of the linear diffusion–migration equation in Eq. (13).

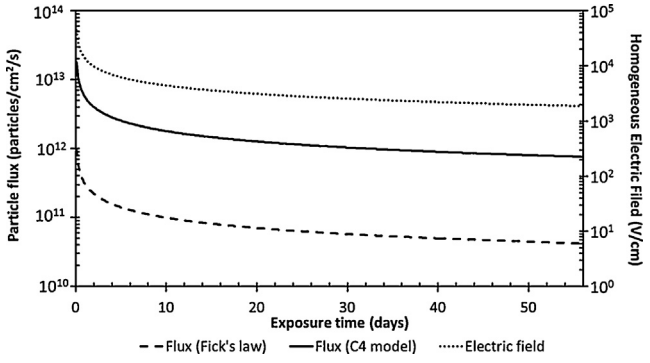

Fig. 6. Vacancy flux (in vacancy/cm^2 s^{-1}) predicted by Fick's law (dotted line) and by the Coupled Current Charge Compensation model (full line) as function of exposure time. The evolution of the homogenous electric field (in V/cm) is also plotted on the right axis.

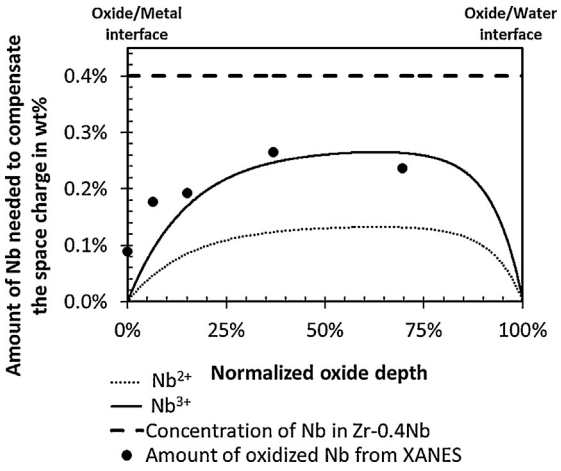

Fig. 7. Amount of oxidized niobium needed to compensate the space charge predicted by the model in Zr–0.4Nb for the two oxidation states Nb^{2+} and Nb^{3+}. The total amount of Nb in Zr–0.4Nb is also plotted (horizontal dotted line). The black points correspond to the amount of oxidized Nb as function of oxide depth determined experimentally by microbeam XANES.

The field modification factor, defined as the ratio of the flux from the C4 model to that from Fick's law is equal to 17, indicating the predominant effect of the electric potential driving force over the concentration gradient driving force on the charged species transport. As expected, the homogeneous electric field decreases as function of exposure time since the oxide grows while the electric potential drop across the oxide is constant.

The subject of the next section is the validity of Eq. (10) from which the parabolic oxidation kinetics is derived.

5.2. Space charge compensation by oxidized Nb

As stated above, in the particular case of Zr–0.4Nb oxidation, the homogeneous field model correctly fits the experimental data. This implies that space charge effect is compensated by Nb in substitution in the oxide layer with a lower valence than Zr^{4+}. The amount in wt% of Nb in substitution needed so that Eq. (10) is verified would be equal to:

$$\omega_{Nb^{m+}}(x_k) = \frac{M_{Nb} \times \left(2C_k^{V_{\ddot{O}}} - C_k^{e^-}\right)}{(4-m) \times N_A \times \rho_{ZrO_2}} \quad (19)$$

where $\omega_{Nb^{m+}}$ is the amount of Nb^{m+} (in wt%) in solid solution in the oxide needed to fully compensate the space charge, M_{Nb} is the molar mass of niobium and ρ_{ZrO_2} is the density of ZrO_2. Since the solid solubility limit of Nb in Zr is higher than 0.4 wt% [66], all Nb is expected to be in solid solution in the metallic Zr–0.4Nb, and it is assumed that this is also true in the oxide. The results for two different Nb oxidation states, $m = 2$ (dotted line) and $m = 3$ (full line), corresponding to NbO and Nb_2O_3 oxides, are plotted in Fig. 7 along with the amount of Nb in Zr–0.4Nb as function of oxide depth (100% being the oxide/water interface). First, because the amount of Nb in solid solution is higher than the amount needed to verify equation (10), it is shown that theoretically there is enough Nb in the Zr–0.4Nb oxide to fully compensate the space charge predicted by the C4 model. Note that only if enough Nb is *actually oxidized*, Eq. (10) would be verified. XANES experiments performed on ZrNb oxide layers corroded in high temperature steam tend to confirm that the Nb oxidation state is lower than 4+ in the oxide layer [67,68] with the possible exception of the oxide/water interface where m is close to 5 [67,69]. In order to characterize the amount of oxidized Nb as function of oxide depth in Zr–0.4Nb alloy, microbeam (0.2 μm spatial resolution) XANES measurements were performed at the

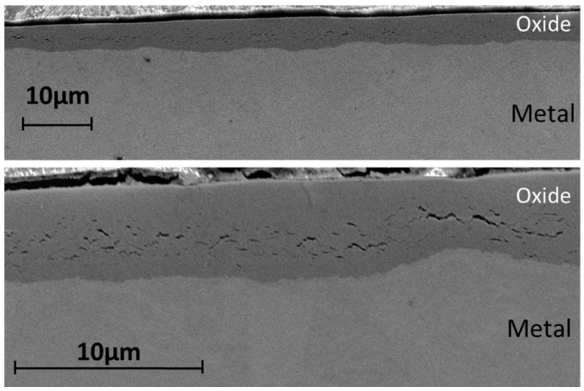

Fig. 8. Scanning Electron Micrographs (secondary electron mode) of cross-sectional Zr–0.4Nb oxide layers ($\delta \sim 4.6$ μm).

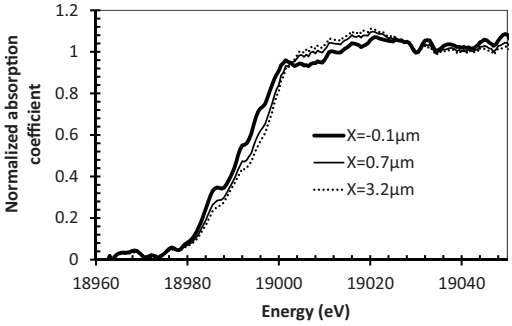

Fig. 9. Normalized fluorescence Nb K-edge XANES spectra acquired at various distances from the oxide/metal interface of a 4.6 μm thick oxide grown on Zr–0.4Nb alloy.

Advanced Photon Source synchrotron (Argonne National Laboratory) on a cross-sectional sample of a 4.6 μm thick Zr–0.4Nb oxide layer (same oxidation kinetics as the sample in Fig. 2), as described in [70]. Scanning Electron Microscope micrographs of this oxide layer are shown in Fig. 8. Although some cracks are present in the oxide as has often been observed in zirconium alloys [71], the oxide appears to be dense overall, with a flat oxide/metal interface, no dendrites or perpendicular cracks being observed. The XANES signals were recorded in fluorescence, with a fluorescence detector placed at approximately 85° from the X-Ray incident beam. The XANES scan energy step is 0.5 eV and the Nb K-edge energy window is 140 eV (from 18.94 keV to 19.08 keV, the edge being located at 18.98 keV). Full details of the microbeam XANES experiment can be found in [70]. Normalized XANES spectra are plotted in Fig. 9 for different oxide depths ($x = 0$ represents the oxide/metal interface and x is positive in the oxide as in Fig. 3). It is clearly observed that the absorption edge shifts to higher energy as the distance from the oxide/metal interface increases, indicating an increase in the oxidized Nb fraction closer to the oxide/water interface. Nb XANES standards have been used to fit the XANES spectra. The library of standards and the fitting method are fully detailed in [70]. In this experiment, it was not possible to discriminate between the different Nb oxidation states but the overall amount of oxidized Nb could be precisely measured at different oxide depths. The results are plotted as black dots in Fig. 7 as function of normalized oxide depth.

Delayed oxidation of Nb relative to Zr when these elements are absorbed in the zirconium oxide layer is observed is in agreement with the literature [70,72]. Microbeam XANES measurements plotted in Fig. 7 confirm that there is enough oxidized Nb to fully compensate the space charge. The experimental results match an overall Nb oxidation state of 3+. In conclusion, the theoretical and

experimental results both confirm the charge compensation effect of Nb in solid solution: oxidized niobium accommodates the extra vacancy charges, reducing the positive space charge in the oxide.

5.3. Discussion and perspectives

If not enough aliovalent ions are present in the oxide to accommodate the extra oxygen vacancy charges, then Eq. (9) is not verified and space charges are not totally compensated. The effect of space charge compensation can be modeled by introducing the space charge compensation factor Γ defined from 0 to 1 as:

$$E(x) = -\frac{dV(x)}{dx} = E_0 + \Gamma\frac{4\pi e}{\varepsilon\varepsilon_0}\int_0^x \left(\sum_s^{\text{diffusing species}} Z_s C_s(x)\right) dx$$
$$= E_0 + \Gamma E_{sp}(x) \quad (20)$$

where E_{sp} is defined as the electric field due to space charge. The charge compensation factor represents the relative amount of aliovalent ions embedded in the oxide compensating a part of the local space charges due to diffusing species (electrons and vacancies). It is recalled that $\Gamma = 0$ is equivalent to Eq. (9) being verified [19]. Thus, the assumption that $\Gamma = 0$ is plausible in the case of Zr–0.4Nb corrosion such that (13) is verified and the homogeneous field approximation leading to parabolic oxidation is justified. If the Nb aliovalent ions *would not be present* then the term ΓE_{sp} *would significantly* affect the oxidation kinetics.

In Zircaloy-type alloys (Zr-1.3Sn-0.2Fe-0.1Cr), the solubility limit of Fe and Cr being at most 200 wt ppm [73], there are not enough Fe and Cr ions in solid solution to compensate space charges in the oxide. It is believed that the electric field induced by the remaining positive space charges in Zircaloy-type alloys would reduce electron transport in the oxide, leading to sub-parabolic oxidation kinetics. The quantitative effect of space charge ($\Gamma \neq 0$) on the oxidation kinetics will be the subject of a following dedicated paper. The effects of Sn and $Zr(Fe,Cr)_2$ precipitates on the space charges in the oxide grown on Zircaloy-type alloys (also not modeled here) are also under investigation.

6. Conclusions

A model of zirconium alloy corrosion during autoclave exposure at 360 °C was developed to investigate the range of sub-parabolic kinetics observed experimentally for different alloying element contents. The Coupled Current Charge Compensation model uses Fromhold's oxidation theory to rationalize the different oxidation kinetics observed by the effect of space charge compensation in the oxide.

1. The Coupled Current Charge Compensation model provides a framework to explain the different oxidation kinetics observed in zirconium alloy corrosion under a single theory based on the space charge compensation by oxidized alloying elements in the oxide. As a first development, the model is fitted to the special case of parabolic oxidation kinetics of ZrNb alloys, assuming that Nb aliovalent ions compensate space charges in the oxide. Under this assumption, the model can reproduce the experimental data using physically significant parameters. The specific results indicate that:
   i. The electron hopping transport occurs via a band of defects (likely oxygen vacancy defects inherently present in the oxide during corrosion) located approximately 1 eV below the conduction band.
   ii. The electric potential driving force is one order of magnitude higher than the concentration gradient driving force and thus needs to be taken into account, in modeling corrosion kinetics. In this study, the electric field lowers the migration energy barrier for vacancy diffusion–migration.
   iii. The vacancy migration energy in the oxide layer is equal to 1.58 eV in agreement with literature results.

   Thus the model fits very well Zr–0.4Nb experimental data assuming that Nb aliovalent ions compensate space charges in the oxide.
2. This outcome can be understood if it is assumed that the oxidized Nb in oxide solid solution compensates the positive space charges in the oxide by accommodating extra oxygen vacancies. Microbeam XANES measurements show that there is enough oxidized Nb in the oxide to compensate the space charges predicted by the model. Thus, both model and experiments support the fact that during ZrNb alloy oxidation, the effect of space charges is compensated by oxidized Nb^{3+} in solid solution, resulting in near parabolic oxidation kinetics. It is expected that in the case of Zircaloy type alloys, not enough oxidized alloying elements would be present in the oxide to compensate space charge, resulting in sub-parabolic kinetics.
3. The model will be applied to the quantitative effect of space charges on the oxidation kinetics in an upcoming publication.

Acknowledgments

Funding for part of this research was provided by the MUZIC-2 (Mechanistic Understanding of Zirconium Corrosion). We are grateful for the support as well as for helpful discussion with Robert Comstock and Javier Romero of Westinghouse, Marc Tupin of CEA and the community of the MUZIC-2 research program.

Appendix A. Verification of the quasi steady state assumption

The hypothesis is that for *a given oxide thickness*, the concentrations of species at any location in the oxide are fixed (instantaneous equilibrium of species as soon as a new oxide monolayer is formed) and do not depend on time. That is, there is no time transient in the concentrations of diffusing species following the formation of a new oxide thickness monolayer. The quasi-steady state limit used in this study corresponds to the particle current case obtained in the theoretical limit in which the boundaries of the oxide film are not moving relative to each other, and following a time lapse sufficient for all transient effects to disappear from the system. In this limit the particle currents are uniform throughout the oxide layer (see Eq. (2)). For another oxide thickness, the oxygen vacancy flux would be different (in the parabolic case it actually varies as $1/\delta$, as detailed in Eq. (C.5)). The fluxes variations as function of exposure time are plotted in Fig. A.1.

It is thus necessary that the time τ_r for a vacancy or an electron to relax in response to a perturbation such as the formation of new oxide is negligible compared to the time to form this given oxide Δt_{ox}:

$$\tau_r \ll \Delta t_{ox} \quad (A.1)$$

Let us verify if this inequality is satisfied in the case studied in the paper.

Δt_{ox} is plotted as function of the oxide monolayer formed in Fig. A.2. As expected, as the oxide grows it takes increasingly more time to form new oxide since oxide growth is limited by atomic species transport. τ_r is determined from Fick's second law of diffusion:

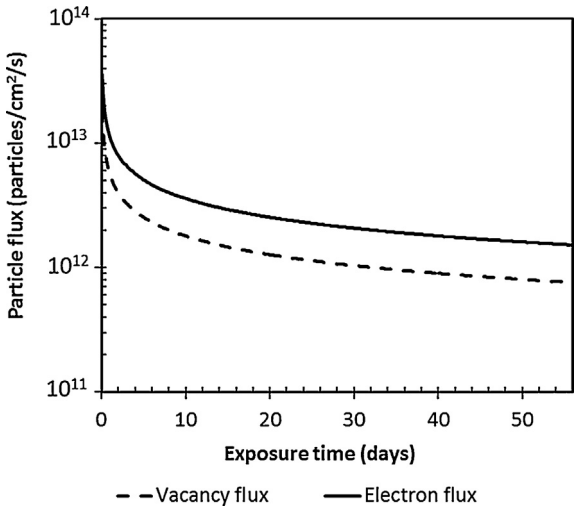

Fig. A.1. Vacancy and electron fluxes as function of exposure time for the Zr–0.4Nb model.

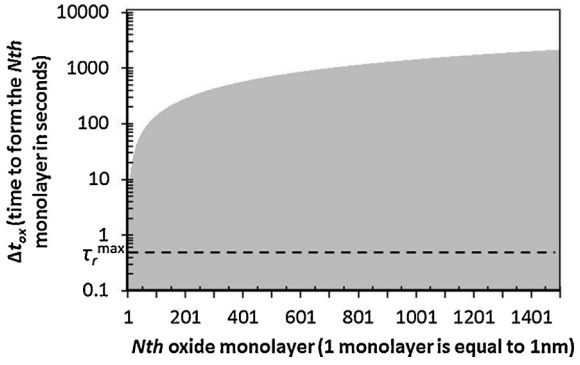

Fig. A.2. Δt_{ox} as function of the oxide monolayer formed.

$$\left(\frac{J_s}{2a\nu_s}e^{\frac{eE^s_m}{k_BT}}\right)\frac{e^{-\left(\frac{Z_seV_{k-1}}{2k_BT}\right)}}{e^{-\left(\frac{Z_seV_k}{k_BT}\right)}} = C^s_{k-1}\left(\frac{e^{-\left(\frac{Z_se\Delta V_{k-1}}{k_BT}\right)}}{e^{-\left(\frac{Z_seV_k}{k_BT}\right)}}\right) - C^s_k\left(\frac{1}{e^{-\left(\frac{Z_seV_k}{k_BT}\right)}}\right)$$
$$= C^s_{k-1}\left(\frac{1}{e^{-\left(\frac{Z_seV_{k-1}}{k_BT}\right)}}\right) - C^s_k\left(\frac{1}{e^{-\left(\frac{Z_seV_k}{k_BT}\right)}}\right) \quad \text{(B.5)}$$

$$\tau_r = \frac{L_r^2}{D} \quad \text{(A.2)}$$

where D is the diffusion coefficient and L_r the corresponding relaxation length. In our study oxygen vacancies have a slower relaxation time (i.e. lower mobility) compared to electrons. From the Einstein relation (assuming $E^{V_{\ddot{O}}}_m = 1.58\,\text{eV}$) the vacancy diffusion coefficient at 360 °C is equal to $D_{V_{\ddot{O}}} = 2.6\times10^{-14}\,\text{cm}^2\,\text{s}^{-1}$. The relaxation length is calculated as the distance at equilibrium between two equal vacancy concentrations for oxides at two successive thickness increments (N and $N+1$ oxide monolayers):

$$C^N_{V_{\ddot{O}}}(x_i) = C^{N+1}_{V_{\ddot{O}}}(x_j) \quad \text{(A.3)}$$

Thus, the relaxation distance L_r is equal to $x_j - x_i$. In the model, this distance never exceeds 1 nm. Thus $\tau_r^{\max} = 0.37s$. $\tau_r^{\max}$ is plotted in Fig. A.2. It is observed that $\tau_r^{\max} \ll \Delta t_{ox}$ is always verified. Thus the quasi steady state hypothesis is correct in the case studied by the model.

Appendix B. Calculation of the Flux of Atomic Species (I)

The change in electrostatic potential between two potential minima k and $k-1$ as depicted in Fig. 3 is approximately given by:

$$\Delta V_{k-1} = V_k - V_{k-1} = -2aE_k \quad \text{(B.1)}$$

with a the jump distance in [m] and E_k the electric field at point k.

Each particle current J^s_k ($s = e^-, V_{\ddot{O}}$) is the difference between the forward current J^{s+}_k due to particles with concentrations C^s_{k-1} jumping from x_{k-1} to x_k through the kth potential maxima with frequency ν_s and the reverse current J^{s-}_k due to the particles with concentrations C^s_k attempting the same barrier jump with the same frequency:

$$J^s_k = J^{s+}_k - J^{s-}_k \quad \text{(B.2)}$$

The barrier height depends on the location of the particles because of the presence of the local electric field E_k such that the barrier height in the forward direction is equal to $E^s_{m_k} - Z_seE_ka$ and to $E^s_{m_k} + Z_seE_ka$ in the reverse direction. Assuming Boltzmann statistics, the particle current J^s_k is equal to:

$$J^s_k = 2a\nu_s e^{-\left(\frac{eE^s_{m_k}}{k_BT}\right)}\left(C^s_{k-1}e^{\frac{Z_seE_ka}{k_BT}} - C^s_k e^{-\left(\frac{Z_seE_ka}{k_BT}\right)}\right) \quad \text{(B.3)}$$

At the steady state limit (see Eq. (2)) and combining Eqs. (B.1) and (B.2):

$$J_s = 2a\nu_s e^{-\left(\frac{eE^s_{m_k}}{k_BT}\right)}\left(C^s_{k-1}e^{-\left(\frac{Z_se\Delta V_{k-1}}{2k_BT}\right)} - C^s_k e^{\frac{Z_se\Delta V_{k-1}}{2k_BT}}\right) \quad \text{(B.4)}$$

Multiplying both sides of Eq. (B.4) by a constant factor and assuming $E^s_{m_k}$ constant across the oxide layer:

By summing Eq. (B.5) from $k=1$ ($k=0$ at the oxide/metal interface) to the oxide/water interface $k=N$ (and considering arbitrarily that $V_0=0$ at the oxide/metal interface as a reference):

$$J_s = 2a\nu_s\frac{\left(C^s_0 - C^s_N e^{\left(\frac{Z_seV_N}{k_BT}\right)}\right)}{e^{\frac{eE^s_m}{k_BT}}\sum_N^{k=1}e^{\left(\frac{Z_se(V_k+V_{k-1})}{2k_BT}\right)}} = g(E, C_s) \quad \text{(B.6)}$$

Nota: the dependence on E arises from $V_k = -\int_0^{ka}E(r)dr$.

It is observed that in the absence of electric field, Eq. (B.6) reduces to Fick's law.

Assuming Eq. (10) is satisfied, the sum in the denominator of the RHS of Eq. (B.6) can be evaluated as:

$$\begin{aligned}\sum_{k=1}^{N} e^{\left(\frac{Z_s e (V_k + V_{k-1})}{2k_B T}\right)} &= \sum_{k=1}^{N} e^{\left(\frac{Z_s e E_0 a (1-2k)}{k_B T}\right)} \\ &= e^{\left(\frac{Z_s e E_0 a}{k_B T}\right)} \times e^{-\left(\frac{2Z_s e E_0 a}{k_B T}\right)} \sum_{k=0}^{N-1} e^{-\left(\frac{2Z_s e E_0 a}{k_B T}\right)^k} \\ &= \frac{e^{-\left(\frac{Z_s e E_0 a}{k_B T}\right)} \left(1 - e^{-\left(\frac{2Z_s e E_0 a}{k_B T}\right)^N}\right)}{1 - e^{-\left(\frac{2Z_s e E_0 a}{k_B T}\right)}} = \frac{1 - e^{-\left(\frac{2NZ_s e E_0 a}{k_B T}\right)}}{2\sinh\left(\frac{Z_s e E_0 a}{k_B T}\right)}\end{aligned} \tag{B.7}$$

Appendix C. Calculation of the Flux of Atomic Species (II)

The analytical solution for the oxidation kinetics is obtained as follows. Let us define a dimensional parameter η as:

$$\eta = e^{\frac{eE_0\delta}{k_B T}} \tag{C.1}$$

The particle current in Eq. (15) can be rewritten as:

$$J_s = \mu_s E_0 \left(\frac{C_N^s - C_0^s(0)\eta^{Z_s}}{1 - \eta^{Z_s}}\right) \tag{C.2}$$

Inserting this equation in the coupled-current equation (7) results in:

$$2\mu_{V_{\ddot{O}}} \left(\frac{C_N^{V_{\ddot{O}}} - C_0^{V_{\ddot{O}}}\eta^2}{1 - \eta^2}\right) - \mu_{e^-} \left(\frac{C_N^{e^-} - C_0^{e^-}\eta^{-1}}{1 - \eta^{-1}}\right) = 0 \tag{C.3}$$

This is a second-degree polynomial equation in η and the unique (positive) physical root is equal to:

$$\eta = \frac{\mu_{e^-}\left(C_0^{e^-} - C_N^{e^-}\right) + \sqrt{\begin{array}{l}\mu_{e^-}^2\left(C_0^{e^-} - C_N^{e^-}\right)^2 - 4 \\ \times\left(\mu_{e^-}C_N^{e^-} - 2\mu_{V_{\ddot{O}}}C_0^{V_{\ddot{O}}}\right)\left(2\mu_{V_{\ddot{O}}}C_N^{V_{\ddot{O}}} - \mu_{e^-}C_0^{e^-}\right)\end{array}}}{2\left(\mu_{e^-}C_N^{e^-} - 2\mu_{V_{\ddot{O}}}C_0^{V_{\ddot{O}}}\right)} \tag{C.4}$$

Rewriting the homogenous electric field using Eq. (C.2), the anion vacancies current is equal to:

$$J_{V_{\ddot{O}}} = \frac{\gamma_{V_{\ddot{O}}}}{\delta}, \text{ with } \gamma_{V_{\ddot{O}}} = \mu_{V_{\ddot{O}}} \frac{k_B T}{e} \ln \eta \left(\frac{C_N^{V_{\ddot{O}}} - C_0^{V_{\ddot{O}}}\eta^2}{1 - \eta^2}\right) \tag{C.5}$$

where $\gamma_{V_{\ddot{O}}}$ is a constant.

Thus the oxidation kinetics is given by:

$$\delta = kt^{0.5}, \text{ with } k = \sqrt{R_v \gamma_{V_{\ddot{O}}}} = f(J_{V_{\ddot{O}}}) \tag{C.6}$$

where R_v is the oxide molecular volume (see Eq. (16)).

References

[1] B. Cox, Some thoughts on the mechanisms of in-reactor corrosion of zirconium alloys, J. Nucl. Mater. 336 (2005) 331–368.
[2] A. Couet, A.T. Motta, R.J. Comstock, Hydrogen pickup measurements in zirconium alloys: relation to oxidation kinetics, J. Nucl. Mater. 451 (2014) 1–13.
[3] H.A. Porte, J.G. Schnizlein, R.C. Vogel, D.F. Fischer, Oxidation of zirconium and zirconium alloys, J. Electrochem. Soc. 107 (1960) 506–515.
[4] A.T. Motta, M.J. Gomes da Silva, A. Yilmazbayhan, R.J. Comstock, Z. Cai, B. Lai, Microstructural characterization of oxides formed on model Zr alloys using synchrotron radiation, in: Zirconium in the Nuclear Industry: 15th International Symposium, ASTM STP 1505, 2009, p. 486.
[5] K. Hauffe, Oxidation of Metals, Plenum Press, 1965.
[6] A.A. Kiselev, Research on the Corrosion of Zirconium Alloys in Water and Steam at High Temperature and Pressure, Atomic Energy of Canada Limited, 1963.
[7] B. Cox, Low temperature (inferior to 300 °C) oxidation of Zircaloy-2 in water, J. Nucl. Mater. 25 (1968) 310–321.
[8] T. Arima, K. Moriyama, N. Gaja, H. Furuya, K. Idemitsu, Y. Inagaki, Oxidation kinetics of Zircaloy-2 between 450 °C and 600 °C in oxidizing atmosphere, J. Nucl. Mater. 257 (1998) 67–77.
[9] J.K. Dawson, G. Long, W.E. Seddon, J.F. White, The kinetics and mechanism of the oxidation of zircaloy-2 at 350–500 °C, J. Nucl. Mater. 25 (1968) 179–200.
[10] M. Tupin, M. Pijolat, F. Valdivieso, M. Soustelle, A. Frichet, P. Barberis, Differences in reactivity of oxide growth during the oxidation of Zircaloy-4 in water vapour before and after the kinetic transition, J. Nucl. Mater. 317 (2003) 130–144.
[11] C. Wagner, W. Schottky, Theory of controlled mixed phases, Z. Phys. Chem. B 11 (1930) 163–210.
[12] J. Robertson, The mechanism of high-temperature aqueous corrosion of steel, Corros. Sci. 29 (1989) 1275–1291.
[13] J.E. Castle, H.G. Masterson, The role of diffusion in the oxidation of mild steel in high temperature aqueous solutions, Corros. Sci. 6 (1966) 93–104.
[14] A.T. Fromhold, Fundamental theory of the growth of thick oxide-films on metals, J. Phys. Soc. Jpn. 48 (1980) 2022–2030.
[15] A.T. Fromhold, Parabolic oxidation of metals in homogeneous electric-fields, J. Phys. Chem. Solids 33 (1972) 95–120.
[16] D.D. Macdonald, The point defect model for the passive state, J. Electrochem. Soc. 139 (1992) 3434–3449.
[17] D.D. Macdonald, The history of the point defect model for the passive state: a brief review of film growth aspects, Electrochim. Acta 56 (2011) 1761–1772.
[18] M. Bojinov, V. Karastoyanov, P. Kinnunen, T. Saario, Influence of water chemistry on the corrosion mechanism of a zirconium–niobium alloy in simulated light water reactor coolant conditions, Corros. Sci. 52 (2010) 54–67.
[19] A.T. Fromhold, Theory of Metal Oxidation: Space Charge, North-Holland, 1980.
[20] A.T. Fromhold, Theory of Metal Oxidation, North Holland Pub. Co, 1975.
[21] G.P. Sabol, S.B. Dalgaard, The origin of the cubic rate law in zirconium alloy oxidation, J. Electrochem. Soc. 122 (1975) 316–317.
[22] H.E. Evans, D.J. Norfolk, T. Swan, Perturbation of parabolic kinetics resulting from the accumulation of stress in protective oxide layers, J. Electrochem. Soc. 125 (1978) 1180–1185.
[23] C.C. Dollins, M. Jursich, A model for the oxidation of zirconium-based alloys, J. Nucl. Mater. 113 (1983) 19–24.
[24] P.J. Shirvington, Electron conduction through oxide films on Zircaloy-2, J. Nucl. Mater. 37 (1970) 177–202.
[25] M.M.R. Howlader, K. Shiiyama, C. Kinoshita, M. Kutsuwada, M. Inagaki, The electrical conductivity of zircaloy oxide films, J. Nucl. Mater. 253 (1998) 149–155.
[26] N. Ramasubramanian, Localised electron transport in corroding zirconium alloys, J. Nucl. Mater. 55 (1975) 134–154.
[27] H. Frank, Transport properties of zirconium alloy oxide films, J. Nucl. Mater. 306 (2002) 85–98.
[28] B. Cox, Oxidation of Zirconium and its Alloys, Plenum, New York, 1976.
[29] B. Cox, Rate controlling processes during the pre-transition oxidation of zirconium alloys, J. Nucl. Mater. 31 (1969) 48–66.
[30] A. Couet, A.T. Motta, R.J. Comstock, Effect of alloying elements on hydrogen pick-up in zirconium alloys, in: B. Comstock (Ed.), 17th International Symposium on Zirconium in the Nuclear Industry, ASTM STP 1543, Hyderabad, India, 2013, pp. 479–514.

[31] Y. Dong, A.T. Motta, E.A. Marquis, Atom probe tomography study of alloying element distributions in Zr alloys and their oxides, J. Nucl. Mater. 442 (2013) 270–281.
[32] C.Y. Chao, L.F. Lin, D.D. Macdonald, A point defect model for anodic passive films: I. Film growth kinetics, J. Electrochem. Soc. 128 (1981) 1187–1194.
[33] T. Pauporte, J. Finne, Impedance spectroscopy study of anodic growth of thick zirconium oxide films in H_2SO_4, Na_2SO_4 and NaOH solutions, J. Appl. Electrochem. 36 (2006) 33–41.
[34] M. Tupin, C. Bataillon, J.-P. Gozlan, P. Bossis, High temperature corrosion of Zircaloy-4, in: R.W. Bosch, D. Féron, J.P. Celis (Eds.), Electrochemistry in Light Water Reactors: Reference Electrodes, Measurement, Corrosion and Tribocorrosion Issues, European Federation of Corrosion, 2007, pp. 134–163.
[35] G.A. Eloff, C.J. Greyling, P.E. Viljoen, The role of space charge in the oxidation of Zircaloy-4 between 350 and 450 °C in air, J. Nucl. Mater. 199 (1993) 285–288.
[36] H.-J. Beie, A. Mitwalsky, F. Garzarolli, H. Ruhmann, H.J. Sell, Examinations of the corrosion mechanism of zirconium alloys, in: Zirconium in the Nuclear Industry: Tenth International Symposium, ASTM STP 1245, Philadelphia, PA, 1994, pp. 615–643.
[37] P. Kofstad, D.J. Ruzicka, On the defect structure of ZrO_2 and HfO_2, J. Electrochem. Soc. 110 (1963) 181–184.
[38] J. Belle, M.W. Mallett, Kinetics of the high temperature oxidation of zirconium, J. Electrochem. Soc. 101 (1954) 339–342.
[39] B. Lustman, F. Kerze, The Metallurgy of Zirconium, McGraw-Hill, 1955.
[40] A. Grandjean, Y. Serruys, Metal and oxygen mobilities during Zircaloy-4 oxidation at high temperature, J. Nucl. Mater. 273 (1999) 111–115.
[41] B. Cox, J.P. Pemsler, Diffusion of oxygen in growing zirconia films, J. Nucl. Mater. 28 (1968) 73–78.
[42] Y. Dali, M. Tupin, P. Bossis, M. Pijolat, Y. Wouters, F. Jomard, Corrosion kinetics under high pressure of steam of pure zirconium and zirconium alloys followed by in situ thermogravimetry, J. Nucl. Mater. 426 (2012) 148–159.
[43] A. Couet, A.T. Motta, A. Ambard, R.J. Comstock, Oxide electronic conductivity and hydrogen pickup fraction in Zr alloys, in: 2014 Annual Meeting on Transactions of the American Nuclear Society and Embedded Topical Meeting: Nuclear Fuels and Structural Materials for the Next Generation Nuclear Reactors, NSFM 2014, ANS Transactions, Reno, NV, USA, 2014, pp. 845–848.
[44] K. Baur, F. Garzarolli, H. Ruhmann, H.-J. Sell, Electrochemical examinations in 350 °C water with respect to the mechanism of corrosion-hydrogen pickup, in: Zirconium in the Nuclear Industry: Twelfth International Symposium, ASTM STP 1354, 2000, pp. 836–852.
[45] N. Ramasubramanian, P. Billot, S. Yagnik, Hydrogen evolution and pickup during the corrosion of zirconium alloys: a critical evaluation of the solid state and porous oxide electrochemistry, in: Zirconium in the Nuclear Industry: Thirteenth International Symposium, ASTM STP 1423, Philadelphia, USA, 2002, pp. 222–244.
[46] H. Gohr, J. Schaller, H. Ruhmann, F. Garzarolli, Long-term in situ corrosion investigation of Zr alloys in simulated PWR environment by electrochemical measurements, in: Zirconium in the Nuclear Industry: Eleventh International Symposium, ASTM STP 1295, 1996.
[47] J. Schefold, D. Lincot, A. Ambard, O. Kerrec, The cyclic nature of corrosion of Zr and Zr-Sn in high-temperature water (633 K) – a long-term in situ impedance spectroscopic study, J. Electrochem. Soc. 150 (2003) B451–B461.
[48] E. Hillner, Hydrogen absorption in Zircaloy during aqueous corrosion, effect of environment, in: AEC Research and Development, 1964.
[49] B. Lustman, M.L. Bleiberg, E.S. Byron, J.N. Chirigos, J.G. Goodwin, G.J. Salvaggio, Zircaloy cladding performs well in PWR, Nucleonics 19 (1961) 58–63.
[50] B.D. Gabory, Y. Dong, A.T. Motta, E.A. Marquis, EELS and atom probe tomography study of the evolution of the metal/oxide interface during zirconium alloy oxidation, J. Nucl. Mater. 462 (2015) 304–309.
[51] A.T. Fromhold, E.L. Cook, Kinetics of oxide film growth on metal crystals: electronic and ionic diffusion in large surface-charge and space-charge fields, Phys. Rev. 175 (1968) 877–897.
[52] D.H. Bradhurst, J.E. Draley, C.J. Van Drunen, An electrochemical model for the oxidation of zirconium, J. Electrochem. Soc. 112 (1965) 1171–1177.
[53] Powder Diffraction File (PDF) Database: Card Nos. 37-1484 monoclinic ZrO_2 in.
[54] A. Charlesby, Electron and photocurrents in thin films of zirconium oxide, Acta Metall. 1 (1953) 348–354.
[55] X. Ma, C. Toffolon-Masclet, T. Guilbert, D. Hamon, J.C. Brachet, Oxidation kinetics and oxygen diffusion in low-tin Zircaloy-4 up to 1523 K, J. Nucl. Mater. 377 (2008) 359–369.
[56] J. Robertson, K. Xiong, S.J. Clark, Band gaps and defect levels in functional oxides, Thin Solid Films 496 (2006) 1–7.
[57] J.G. Simmons, Poole–Frenkel effect and Schottky effect in metal-insulator-metal systems, Phys. Rev. 155 (1967) 657–660.
[58] W.S. Chan, C.K. Loh, Electrical conduction of zirconium oxide films, Thin Solid Films 6 (1970) 91–105.
[59] K.N. Nikitin, A.G. Atanasyants, A.A. Emel'yanov, Electroconduction in the $ZrIZrO_2I$ electrolyte system, Russ. J. Electrochem. 42 (2006) 398–402.
[60] M. Uno, K. Takahashi, T. Nakayama, S. Yamanaka, Photoelectrochemical study of hydrogen in oxide films of Zr based alloys for fuel cladding materials of light water reactors, J. Alloys Compd. 446 (2007) 635–638.
[61] Y. Isobe, M. Fuse, K. Kobayashi, Additive element effects on electronic conductivity of zirconium-oxide film, J. Nucl. Sci. Technol. 31 (1994) 546–551.
[62] T. Smith, Diffusion coefficients and anion vacancy concentrations for zirconium–zirconium dioxide system, J. Electrochem. Soc. 112 (1965) 560–567.
[63] F.G. Ullman, Photoconduction and trapping in sputtered tantalum oxide films, J. Phys. Chem. Solids 28 (1967) 279–289.
[64] U. Brossmann, R. Wurschum, U. Sodervall, H.-E. Schaefer, Oxygen diffusion in ultrafine grained monoclinic ZrO_2, J. Appl. Phys. 85 (1999) 7646–7654.
[65] O.I. Malyi, P. Wu, V.V. Kulish, K. Bai, Z. Chen, Formation and migration of oxygen and zirconium vacancies in cubic zirconia and zirconium oxysulfide, Solid State Ionics 212 (2012) 117–122.
[66] J.P. Abriata, J.C. Bolcich, The Zr–Nb (zirconium–niobium) system, Bull. Alloy Phase Diag. 3 (1982) 1710–1712.
[67] K. Sakamoto, K. Une, M. Aomi, K. Hashizume, Oxidation behavior of Niobium in oxide layers of zirconium–niobium alloys, in: Top Fuel 2012, Manchester, UK, 2012, pp. 297–306.
[68] A. Froideval, C. Degueldre, C.U. Segre, M.A. Pouchon, D. Grolimund, Niobium speciation at the metal/oxide interface of corroded niobium-doped Zircaloys: a X-ray absorption near-edge structure study, Corros. Sci. 50 (2008) 1313–1320.
[69] P. Bossis, D. Pecheur, K. Hanifi, J. Thomazet, M. Blat, Comparison of the high burn-up corrosion on M5 and low tin zircaloy-4, in: Zirconium in the Nuclear Industry: Fourteenth International Symposium, ASTM STP 1467, 2005, pp. 494–524.
[70] A. Couet, A.T. Motta, B. de Gabory, Z. Cai, Microbeam X-ray absorption near-edge spectroscopy study of the oxidation of Fe and Nb in zirconium alloy oxide layers, J. Nucl. Mater. 452 (2014) 614–627.
[71] A. Yilmazbayhan, A.T. Motta, R.J. Comstock, G.P. Sabol, B. Lai, Z. Cai, Structure of zirconium alloy oxides formed in pure water studied with synchrotron radiation and optical microscopy: relation to corrosion rate, J. Nucl. Mater. 324 (2004) 6–22.
[72] D. Pêcheur, Oxidation of β-Nb and $Zr(Fe,V)_2$ precipitates in oxide films formed on advanced Zr-based alloys, J. Nucl. Mater. 278 (2000) 195–201.
[73] A. Yilmazbayhan, O. Delaire, A.T. Motta, R.C. Birtcher, J.M. Maser, B. Lai, Determination of the alloying content in the matrix of Zr alloys using synchrotron radiation microprobe X-ray fluorescence, J. Nucl. Mater. 321 (2003) 221–232.
[74] N.F. Mott, The theory of the formation of protective oxide films on metals: 3, Trans. Faraday Soc. 43 (1947) 429–434.
[75] N. Cabrera, N.F. Mott, Theory of the oxidation of metals, Rep. Prog. Phys. 12 (1948) 163–184.
[76] A. Seyeux, V. Maurice, P. Marcus, Oxide film growth kinetics on metals and alloys I. Physical model, J. Electrochem. Soc. 160 (2013) C189–C196.
[77] K. Leistner, C. Toulemonde, B. Diawara, A. Seyeux, P. Marcus, Oxide film growth kinetics on metals and alloys II. Numerical simulation of transient behavior, J. Electrochem. Soc. 160 (2013) C197–C205.
[78] C. Bataillon, F. Bouchon, C. Chainais-Hillairet, C. Desgranges, E. Hoarau, F. Martin, S. Perrin, M. Tupin, J. Talandier, Corrosion modelling of iron based alloy in nuclear waste repository, Electrochim. Acta 55 (2010) 4451–4467.
[79] C. Bataillon, F. Bouchon, C. Chainais-Hillairet, J. Fuhrmann, E. Hoarau, R. Touzani, Numerical methods for the simulation of a corrosion model with moving oxide layer, J. Comput. Phys. 231 (2012) 6213–6231.
[80] S. Forsberg, E. Ahlberg, M. Limback, Studies of corrosion of cladding materials in simulated BWR environment using impedance measurements, in: Zirconium in the Nuclear Industry: 15th International Symposium, ASTM STP 1505, W Conshohocken, 2009, pp. 303–325.
[81] D.A. Vermilyea, Electron and photocurrents in thin films of ZrO_2, Acta Metall. 2 (1954) 346–348.